

# Sn ion energy distributions of ns- and ps-laser produced plasmas

A Bayerle<sup>1</sup> , M J Deuzeman<sup>1,2</sup>, S van der Heijden<sup>1</sup>, D Kurilovich<sup>1,3</sup> ,  
T de Faria Pinto<sup>1</sup>, A Stodolna<sup>1</sup>, S Witte<sup>1,3</sup>, K S E Eikema<sup>1,3</sup>, W Ubachs<sup>1,3</sup>,  
R Hoekstra<sup>1,2</sup> and O O Versolato<sup>1</sup> 

<sup>1</sup>Advanced Research Center for Nanolithography (ARCNL), Science Park 110, 1098 XG Amsterdam, The Netherlands

<sup>2</sup>Zernike Institute for Advanced Materials, University of Groningen, Nijenborgh 4, 9747 AG Groningen, The Netherlands

<sup>3</sup>Department of Physics and Astronomy and LaserLab, Vrije Universiteit Amsterdam, De Boelelaan 1081, 1081 HV Amsterdam, The Netherlands

E-mail: [o.versolato@arcnl.nl](mailto:o.versolato@arcnl.nl)

Received 31 October 2017, revised 13 February 2018

Accepted for publication 8 March 2018

Published 4 April 2018



CrossMark

## Abstract

Ion energy distributions arising from laser-produced plasmas of Sn are measured over a wide laser parameter space. Planar-solid and liquid-droplet targets are exposed to infrared laser pulses with energy densities between  $1 \text{ J cm}^{-2}$  and  $4 \text{ kJ cm}^{-2}$  and durations spanning 0.5 ps to 6 ns. The measured ion energy distributions are compared to two self-similar solutions of a hydrodynamic approach assuming isothermal expansion of the plasma plume into vacuum. For planar and droplet targets exposed to ps-long pulses, we find good agreement between the experimental results and the self-similar solution of a semi-infinite simple planar plasma configuration with an exponential density profile. The ion energy distributions resulting from solid Sn exposed to ns-pulses agrees with solutions of a limited-mass model that assumes a Gaussian-shaped initial density profile.

Keywords: plasma expansion, laser-produced plasma, ion energy

## 1. Introduction

Plasma expansion into vacuum is a subject of great interest for many applications ranging from ultracold plasmas [1, 2] over laser acceleration [3, 4] to short-wavelength light sources [5, 6]. For such light sources driven by laser-produced plasmas (LPPs), the optics that collect the plasma-generated light are exposed to particle emission from the plasma. The impinging particles may affect the performance of the light-collecting optics.

Charged particles from LPPs can be monitored by means of Faraday cups (FCs)—a robust plasma diagnostics tool. Faraday cups can be used to characterize the angular distribution of ion emission of metal and non-metal LPPs [7, 8].

Faraday cups in the time-of-flight mode can be used to measure the energy distributions of the ions emanating from the plasma interaction zone [9–11]. Because of its relevance to extreme ultraviolet nanolithography, the LPP of Sn has been the subject of similar studies, in which the kinetic energy and yield of the Sn ions together with the extreme-ultraviolet light output are characterized [12]. Indications of a set of laser parameters were reported for which a dip in the Sn ion yield might occur [13]. Both droplet and planar targets have been investigated [14, 15] but no unique optimal conditions have been found so far.

In order to understand the ion energy distributions from LPPs, a theoretical framework based on hydrodynamic expansion has been established early on [16, 17]. The theoretical framework has been expanding ever since. Nevertheless, benchmarking the energy distribution functions derived in the different studies with the experimental data on LPPs remains scarce. To the best of our knowledge, only two groups have reported the comparison of the results of hydrodynamics models to ion energy distributions measured by FCs [18, 19].

 Original content from this work may be used under the terms of the [Creative Commons Attribution 3.0 licence](https://creativecommons.org/licenses/by/3.0/). Any further distribution of this work must maintain attribution to the author(s) and the title of the work, journal citation and DOI.

Laser-produced plasmas can be created over a vast space of laser and target parameters. Here, we address the energy distributions of emitted ions in a substantial subset of this space, namely pulse lengths ranging from sub-ps to almost 10 ns and laser peak fluences up to  $3 \text{ kJ cm}^{-2}$ . The plasma is produced on solid-planar and liquid-droplet targets irradiated by infrared lasers. The measured results are used to benchmark two analytical solutions of hydrodynamics models of plasma expansion into vacuum [19, 20]. The intended accuracy of this comparison between theory and our experiments is not expected to be able to discern any effects beyond those predicted by these single-fluid single-temperature hydrodynamic plasma models, such as the possible presence of a double layer [20–22]. First, the solution to a semi-infinite simple planar model, assuming an exponential density profile of the plasma [20], shows good agreement with the experimental results of the LPP by ps-laser pulses. Second, the ion energy distributions obtained by exposing solid Sn targets to 6-ns laser pulses agree best with the solution to a modified hydrodynamics model [19]. In that work, a different density evolution of the expanding plasma is derived, starting out from a Gaussian density profile instead of the exponential profile, used in the work of Mora [20]. In addition, the modified model takes into account the dimensionality of the plasma expansion.

In section 3, the experimental setups used to produce Sn plasmas by pulsed lasers are described. The ion energy distributions are shown in section 4. We compare the ion energy distributions with the results of theoretical studies on plasma expansion into vacuum, which are briefly reviewed in the following section 2.

## 2. Theoretical models

Plasma expansion into vacuum traditionally is treated by a hydrodynamic approach [16]. A typical initial condition consists of cold ions with a charge state  $Z$  and a hot gas of electrons with energies distributed according to Maxwell-Boltzmann [23]. The electron cloud overtakes the ions during expansion, leading to an electrostatic potential that accelerates the ions. The hydrodynamic equations of plasma expansion can be solved by a self-similar ansatz with the coordinate  $x/R(t)$ , where  $x$  is the spatial coordinate and  $R(t) = c_s t$  [20] or  $R(t) \propto t^{1.2}$  [19] is the characteristic system size growing with the sound speed  $c_s$ . Many theoretical studies that are based on such a hydrodynamics approach solve the problem of plasma expansion into vacuum by making different assumptions, for example, isothermal or adiabatic expansion [24] or a non-Maxwellian distribution of the electrons [25, 26]. Here, we focus on two studies published by Mora [20] and Murakami *et al* [19] where we assume that the charge state  $Z$  can be interpreted as an average charge state. This presents a strong simplification, especially in our rapidly expanding laser-driven plasma containing multiply charged ions (see e.g. [27, 28]). Our FC technique cannot resolve ions by their charge and the measured distribution is in fact a convolution of distributions of ions of the various charge

states. These energy distributions may be expected to depend on charge state  $Z$  (see e.g. [21, 29]) and the collected charge on the FC is  $Z$  times the amount of ions captured. Nevertheless, it is instructive to compare the charge-per-ion energy distributions measured on FCs with the solutions to these single-fluid single-temperature hydrodynamic plasma models in terms of emitted particle number per energy interval. In Mora [20], the particle energy distribution is found to be

$$dN/dE \propto (E/E_0)^{-1/2} \exp(-\sqrt{E/E_0}), \quad (1)$$

while Murakami *et al* [19] derives

$$dN/dE \propto (E/\tilde{E}_0)^{(\alpha-2)/2} \exp(-E/\tilde{E}_0), \quad (2)$$

under inclusion of higher dimensionality  $\alpha$  and Gaussian evolution of the density.

The respective ion energies are characterized by  $E_0$  or  $\tilde{E}_0$ . The characteristic energy depends on the charge state  $Z$  of the ions and the electron temperature  $T_e$ . In the first equation, the characteristic ion energy  $E_0$  is given by

$$E_0 = Zk_B T_e, \quad (3)$$

with  $k_B$  the Boltzmann constant. The ion energy in equation (2) is given by

$$\tilde{E}_0 = m\dot{R}^2(t)/2 = 2Zk_B T_e \ln(R(t)/R_0), \quad (4)$$

with  $m$  the ion mass and  $R_0$  the initial size. A higher  $E_0$  or  $\tilde{E}_0$  means there are relatively more high-energy ions, with a higher mean charge state and a higher electron temperature.

Both models assume Boltzmann-distributed electron energies and isothermal expansion of the plasma. Additionally, in [19], the solution (our equation (2)) is extended and smoothly connected with a solution of an adiabatically expanding plasma. The resultant ion energy spectrum is given in the same form as our equation (2), only with a slight modification in the characteristic energy scale  $\tilde{E}_0 \rightarrow f\tilde{E}_0$ . For simplicity, we use the solution in their first step to analyze our experimental results.

One essential difference between the two models is the functional form of the density evolution of the expanding plasmas. In [20], the charge density is obtained as a perturbation of the initial charge density, which then evolves as  $n \propto \exp(-x/R(t))$  (see also [30]). In [19], the authors argue that for longer pulse lengths or limited target masses, this perturbation assumption is not valid. They obtain a Gaussian form for the charge density profile [31, 32]:  $n \propto \exp(-(x/R(t))^2)$ . This density profile results in a different high-energy tail of the ion distribution. The dimensionality is captured by the parameter  $\alpha$ . If  $\alpha = 1$ , the expansion is planar, otherwise the expansion is cylindrical or spherical for  $\alpha = 2$  and  $\alpha = 3$ , respectively.

## 3. Experimental setup

We use two setups to create laser-produced plasmas of Sn and measure the energy distributions of the emitted ions. Figure 1(a) shows the schematic representation of the setups. The first setup contains a solid Sn plate of 1 mm thickness as

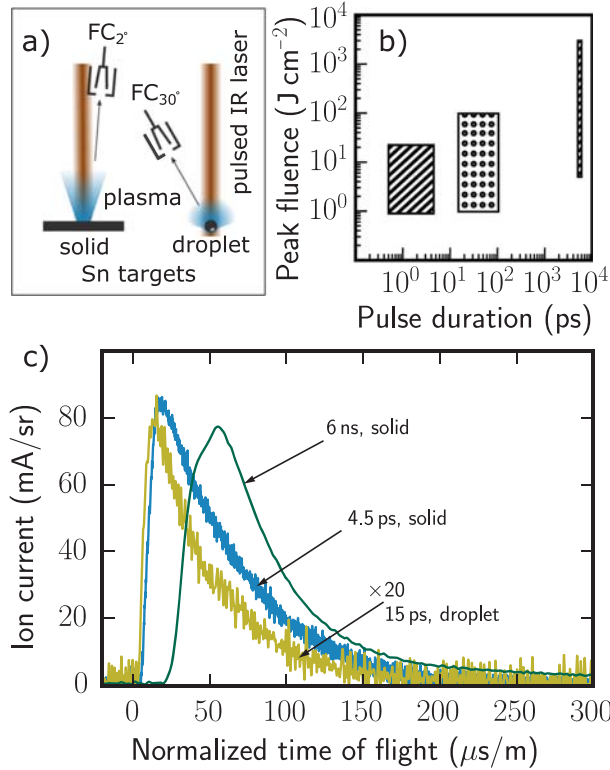


**Figure 1.** (a) Schematic of the experimental setups. The plasma is created by exposing Sn metal targets to focused infra-red laser pulses. The Sn target has either planar geometry (solid target) or consists of droplets of  $30\ \mu\text{m}$  diameter. The ion emission is collected by Faraday cups (FC) that are roughly 1 m away from the plasma source. (b) Pulse duration and peak fluence parameter space addressed by the experiments. Hatched rectangles show the parameter space explored using solid targets. The parameter space explored on Sn droplets is shown by the dotted rectangle. (c) Typical examples of time dependent ion traces collected by the FCs. The x-axis is normalized to a time-of-flight distance of 1 m. The targets are exposed to fluences of  $25\ \text{J cm}^{-2}$  (solid target) and  $30\ \text{J cm}^{-2}$  (droplet target).

a target. In the second experiment, the targets are free falling droplets of molten Sn with a diameter of  $30\ \mu\text{m}$ . The solid and droplet targets reside in vacuum apparatuses with base pressures below  $10^{-6}$  mbar. Pulsed infrared laser beams are focused on the targets to create the plasma. The ion emission is collected by FCs mounted into the vacuum apparatus around the plasma.

The custom-made FCs consist of a cone shaped charge collecting electrode, mounted behind a suppressor electrode [15]. Both electrodes are housed in a grounding shield. The FCs have an opening of 6 mm diameter and are mounted at a distances between 25 cm and 75 cm. The collector and suppressor are biased to a negative potential with respect to ground in order to prevent plasma electrons from entering the cup, and secondary electrons from leaving the cup after Sn ions impinge on the surface of the collector.

Faraday cup measurements can only serve to give an approximation of the plasma flow as the separation of

electrons from the ions in the quasi-neutral expansion of the plasma cannot be assumed to be complete and may depend on the set bias voltages and earth magnetic fields [33]. We verified that further increasing the bias voltages had no significant impact on the measured time-of-flight traces. The earth magnetic field is only expected to influence the detection of low-energy ions.

Figure 1(c) shows typical time-of-flight traces acquired by the FCs during experimental runs. The ion current is measured across a shunt resistor with a digital storage oscilloscope. The traces are averaged for the same laser fluence for about hundred laser exposures. The ns-laser produced traces have a lower noise amplitude, because the traces are averaged for about two hundred exposures. The shunt resistor of  $10\ \text{k}\Omega$ , the added capacitance of  $220\ \text{pF}$  of the collector cup and the cable to the oscilloscope form an RC-network that limits the bandwidth of the measurement. The effective RC-time of the read-out is on the order of  $2\ \mu\text{s}$ . In order to retrieve the ion current from the raw data, we correct for the response function of the read-out network. The ion traces can be integrated in time to obtain the total charge emitted into the direction of the corresponding FC. The energy distribution can be calculated by the following transformation

$$dQ/dE = t^3 I(E)/mL, \quad E = mL^2/2t^2,$$

with  $m$  the mass of Sn,  $L$  the distance between the plasma and the detector and  $t$  the time-of-flight. The charge yield per energy interval is averaged over bins of  $10\ \text{eV}$ .

As shown in figure 1(c), the time-of-flight traces for pulses below 15 ps have a smaller signal-to-noise ratio. The traces converge to the background noise level at  $170\ \mu\text{s/m}$ . This time-of-flight is equivalent to an energy of  $20\ \text{eV}$ . Therefore, we truncate the energy distributions below  $20\ \text{eV}$ .

The setup containing the droplet target is described in detail by Kurilovich *et al* [34]. The Sn droplets are created by pushing liquid Sn through a piezo-driven orifice. The orifice diameter and piezo driver frequency determine the diameter of the droplets to  $30\ \mu\text{m}$ . A pulsed 1064-nm Nd:YAG laser is focused to a  $100\ \mu\text{m}$  full width at half maximum (FWHM) Gaussian spot at the position of the droplet stream. Faraday cups are added at 37 cm under angles of  $30^\circ$  and  $60^\circ$  with respect to the incoming laser beam to enable time-of-flight measurements.

The second setup containing the solid target is described in detail by Deuzeman *et al* [15]. The solid target is mounted onto a 2D-translation stage (PI miCos model E871) enabling a computer-controlled, stepwise motion of the target between laser pulses in a perpendicular direction to the laser beam. The stepwise translation of the target between pulses is necessary to prevent the ion emission to change because of surface deformation after too many laser shots on the same spot. Also, the first few laser pulses on a new spot on the surface ablate the oxide layer and the subsequent laser pulses produce plasmas containing mostly Sn [35]. Two laser systems are employed to create plasma at the Sn solid surface. First, a 800-nm wavelength Ti:sapphire laser is used to generate pulses of 0.5ps to 4.5 ps duration. The Gaussian spot size of

the the 800-nm laser at the surface of the target is  $100\ \mu\text{m}$  FWHM. Second, a Nd:YAG laser outputs 6-ns long pulses. This laser has a wavelength of 1064 nm and is focused to a Gaussian spot of  $90\ \mu\text{m}$  FWHM. The setup is equipped with three FCs, one at a distance of 73 cm and at an angle of  $2^\circ$  from the surface normal, and two at  $\pm 30^\circ$  at distances of 26 cm and 73 cm.

We summarize the laser parameter space accessible with the lasers in figure 1(b). The peak fluence and pulse duration used in the experiments performed on a solid target are shown as hatched rectangles. The Ti:sapphire laser produces ultrashort pulses ranging from 0.5 ps to 4.5 ps without evidence for intensity-induced self-focusing or self-phase modulation effects. Peak pulse energy densities run up to  $30\ \text{J cm}^{-2}$ . The pulse length of the Nd:YAG laser used on the solid target is 6 ns and the pulse energy densities reach  $3\ \text{kJ cm}^{-2}$ . The dotted rectangles shows the parameter space for the experiments on droplets. The Nd:YAG laser employed in the droplet setup is capable of producing ultrashort pulses between 15 ps and 105 ps duration and peak fluences of 1 to  $100\ \text{J cm}^{-2}$ .

## 4. Results and discussion

First, we present the energy distributions of the Sn ion emission for three different pulse lengths and same energy density of the laser and show that the experimental data can be well described by the self-similar solutions of the hydrodynamic model. Second, we show the ion distributions obtained for different laser fluences and for fixed pulse durations.

### 4.1. Changing pulse duration

We measure the ion energy distributions on the different target geometries with the following laser parameters. The solid target is irradiated by 6-ns, 1064-nm and 4.5-ps, 800-nm pulses with a peak fluence of  $25\ \text{J cm}^{-2}$  and the Sn droplets are exposed to 15-ps and 105-ps pulses with a peak fluence of  $30\ \text{J cm}^{-2}$  and 1064 nm wavelength. The presented ion energy distributions are measured under different angles for the two target geometries. Ion emission from the solid target is measured at  $2^\circ$  (and  $30^\circ$ , see Deuzeman *et al* [15]) with respect to the surface normal, while the droplet target emission is collected by the FC mounted at an angle of  $30^\circ$  from the laser axis. Because most (and most energetic) ions are emitted along the surface normal [28, 36, 37], the ion emission in the  $30^\circ$  direction from the spherical droplet target (thus emitted along a surface normal) is best compared to the ion emission in the small-angle,  $2^\circ$  direction from the planar target. In this comparison, we note that the projection of the laser beam onto the droplet surface at a  $30^\circ$  angle-of-incidence will reduce the local fluence by the cosine of this angle. The absorption, governed by the Fresnel equations, also depends on this angle. Both effects, however, have minor impact, considering the relatively small angle involved and, in fact, these two effects partially cancel each other (see e.g.

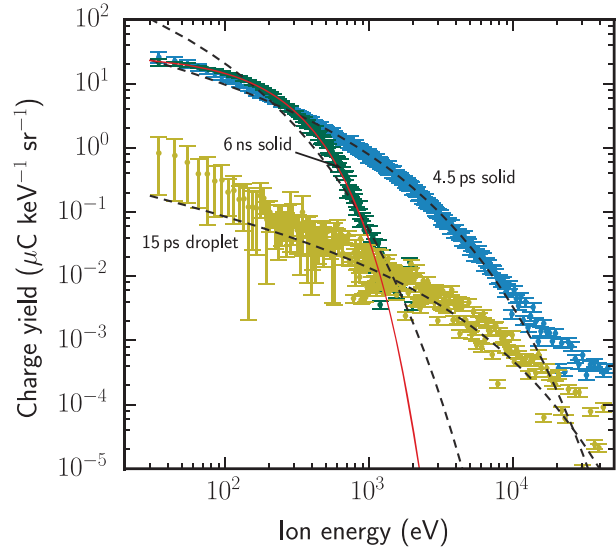


**Figure 2.** Charge energy distributions measured for different pulse durations of the laser on both solid-planar and liquid-droplet targets. The energy density of the laser pulses is  $25\text{--}30\ \text{J cm}^{-2}$ . The dashed (black) lines show the fits of equation (1) to the distributions. The solid (red) line is a fit of equation (2) with  $\alpha = 2$  to the data.

[38]). The difference in the reflectivities between solid and liquid tin before the laser impact is quite small at 2 percentage points, comparing 82 to 84%, respectively (taking as input, the works of [39, 40]). At our typical energy fluences, however, the solid target is practically instantaneously melted and heated to several thousand degrees (within the skin layer). Thus, the target reflectivity, identically for both solid planar and liquid droplet cases, is determined by the optical properties of liquid and vaporized tin at  $T \sim 3000\ \text{K}\text{--}5000\ \text{K}$  that are poorly known and quite different from those at room temperature.

Figure 2 shows the ion energy distributions of the LPPs obtained with the laser parameters described above. In all cases, the charge yields decrease monotonically with ion energy. Charge yields obtained from pulses below 6-ns duration converge and hit the detection threshold around an ion energy of 30 keV. Long laser pulses of 6 ns produce charge yields that roll off already at 1 keV at a faster rate.

For ps-pulses, the charge yield retrieved from the solid target is more than an order of magnitude higher than from the droplet target for energies below 5 keV. For the solid target, we acquire a total charge of about  $4\ \mu\text{C/sr}$  and  $3\ \mu\text{C/sr}$  for 4.5-ps and 6-ns pulse length, respectively. The droplet target yields a total charge of only  $0.06\ \mu\text{C/sr}$  when exposed to the 15-ps laser pulse. We attribute this difference between collected charge to the smaller droplet diameter compared to the focused laser beam diameter. While the solid target is irradiated by a full Gaussian intensity profile, the droplet is exposed to only a fraction of the focused laser beam energy because the diameter of the droplet is three times smaller than the FWHM of the beam. The energy deposited on the droplet can be calculated by integrating the Gaussian beam fluence

profile over the droplet. Then, the energy on the droplet is  $E_d = E_L(1 - 2^{-d_D^2/d_L^2})$  with  $d_D$  the droplet diameter,  $E_L$  and  $d_L$  the total laser energy and the FWHM diameter of the focused laser beam. For our experimental parameters, the droplet is exposed to only 6% of the total laser energy and thus the observed total charge yield will be substantially smaller than from the solid target.

The energy distributions of figure 2 are compared with the theoretical predictions discussed above. The dashed (black) lines show the least-squares fitted energy distributions according to equation (1) for pulse lengths of 4.5 ps and 15 ps. The experimental energy distributions agree well with equation (1) for both target geometries and slightly different wavelengths. Applying the model comparison yields the characteristic ion energy  $E_0$ . For the 4.5-ps LPP, we obtain  $E_0 = 250(30)$  eV.

Model comparisons of the energy distributions of Sn ions emitted from the droplet target give higher characteristic energies. The plasma produced by the 15-ps laser pulses with  $30 \text{ J cm}^{-2}$  energy density yields  $E_0 = 970(120)$  eV. This higher characteristic energy could well be the result of the irradiation of the droplet by only the central fraction of the laser beam where the fluence is highest. The droplet is exposed to the central 6% of the total laser energy, therefore the average fluence is close to the peak fluence and thus exceeds the one on the solid target.

Irradiating the solid target surface with the 6-ns laser pulses produces an energy distribution that does not agree with equation (1), as illustrated in figure 2 by the dashed (black) line. The fit of equation (2) to the measured energy distribution is shown as a solid (red) line in figure 2. The dimensionality parameter is set to  $\alpha = 2$  and with a characteristic ion energy of  $\tilde{E}_0 = 150(15)$  eV, the model agrees well with the measured distributions.

The energy distributions of LPP Sn ions are reproduced well in the energy interval of 20 eV to 20 keV, although the target geometries and pulse durations vary significantly. Laser produced plasmas of ps-pulses show good agreement with equation (1), and can thus be modelled by the approach of Mora [20]. Between 100 ps and 6 ns pulse duration, the ablated target material starts to absorb the laser energy and the density profile deviates from  $\rho \propto \exp(-x/R(t))$ . In this case, we cannot expect equation (1) to fit the data. Instead, the experimental energy distribution for the 6-ns laser produced plasma is well described by equation (2).

In the following, we focus on the study of the applicability of the two introduced models over the measured range of laser energy densities.

#### 4.2. Changing laser energy density

In the following, we explore the applicability of the two models to ion energy distributions obtained from LPPs at different energy densities of the laser and fixed pulse durations.

The solid target is exposed to 4.5-ps pulses from the Ti:sapphire laser with different energy densities. The resulting charge energy distributions are shown in figure 3(a). The four

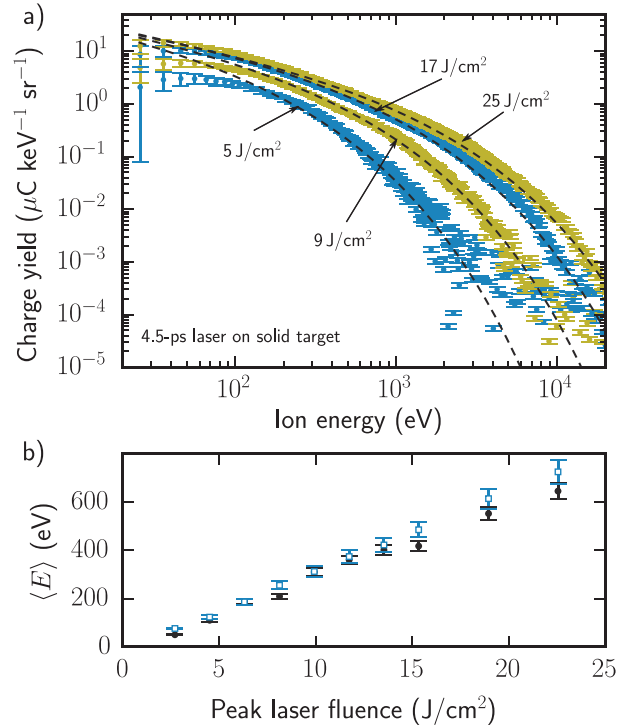


**Figure 3.** (a) Charge energy distributions for a pulse duration of 4.5 ps and different laser energy densities on the solid target, and fits with equation (1). (b) The values for  $2E_0 = \langle E_{\text{fit}} \rangle$  (solid, black circles) obtained from the fits with equation (1) for these distributions, with  $\langle E_{\text{exp}} \rangle$  (open, blue squares).

plots on the top are acquired by the FC at  $2^\circ$ . These energy distributions are fit with equation (1) and shown as dashed (black) lines. It is informative to also compare the average kinetic energies obtained from the fits  $\langle E_{\text{fit}} \rangle$  to those obtained directly from the data  $\langle E_{\text{exp}} \rangle$ , enabling us to judge how accurately the theories describe the experiments. The average energy  $\langle E_{\text{fit}} \rangle = 2E_0$  and  $\langle E_{\text{fit}} \rangle = \tilde{E}_0/2$  for  $\alpha = 1$  can be obtained from equations (1) and (2) analytically, but as a correction related to the low-energy, 20 eV cut-off needs to be applied to the values  $\langle E_{\text{exp}} \rangle$ . The corresponding correction factor ranging from 1.2 to 1.6 is obtained by comparing the energy averages of equations (1) and (2) from zero to infinity and from 20 eV and infinity. The correction factor is applied to  $\langle E_{\text{exp}} \rangle$  in the following. We find good agreement between the obtained values as presented in figure 3(b).

Exposing the droplets to ultrashort pulses of 15 ps duration results in similar energy distributions as for the solid target. Figure 4(a) shows the distributions for increasing energy density of the laser pulse. The distributions are fit with equation (1) and plotted as dashed (black) lines. The agreement between the experimental distributions and the model is good for ion energies below 10 keV. For high energy densities of the laser ( $>20 \text{ J cm}^{-2}$ ), equation (1) underestimates the amount of ions with energies above 10 keV. Again, the characteristic ion energies are plotted in dependence of the peak laser fluence in figure 4(b). Below peak fluences of  $40 \text{ J cm}^{-2}$  of the laser, the characteristic ion energies increase.

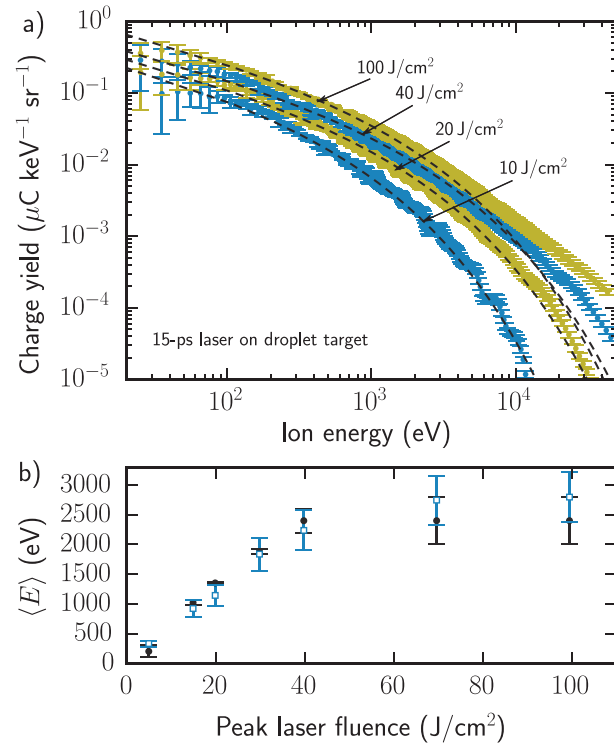


**Figure 4.** (a) Charge yield distributions for different energy densities of the laser on the Sn droplets and fits with equation (1). (b) The values for  $2E_0 = \langle E_{\text{fit}} \rangle$  (solid, black circles) obtained from the fits with equation (1) for these distributions, with  $\langle E_{\text{exp}} \rangle$  (open, blue squares).

At higher peak fluence ( $100 \text{ J cm}^{-2}$ ), the fit misses the high-energy tail of the distribution. As a result, the value for  $E_0$  obtained from the fit appears to saturate at 1.2 keV. We find good agreement between the obtained values  $\langle E_{\text{exp}} \rangle$  and  $\langle E_{\text{fit}} \rangle$  (see figure 4).

The charge distributions change significantly when we use the 6-ns instead of the ps-laser pulses to produce the plasma. Figure 5(a) shows the energy distributions derived from the time-of-flight traces of the ions emitted from the solid target at an angle of  $2^\circ$ . The distributions are measured at peak fluences of the laser pulses ranging from  $23.5 \text{ J cm}^{-2}$  to  $3 \text{ kJ cm}^{-2}$ . Fitting the distributions with equation (2) requires us to set an appropriate dimensionality parameter  $\alpha$ . The parameter is determined by the ratio of the typical plasma flow length scale and the size of the laser spot size [19]. In our experiments, this length scale and laser focus are of a similar size and thus the choice of the dimension is not straightforward. We find that setting  $\alpha = 1$  or 2 gives satisfactory agreement with the obtained data in the following. To determine the actual dimensionality of the expanding plasma, further measurements are required over a range of laser spot sizes with a multi-angle and charge-state-resolved approach. With the dimensionality parameter set to  $\alpha = 1$ , the energy distributions produced by pulses of laser fluences between  $80 \text{ J cm}^{-2}$  and  $1.6 \text{ kJ cm}^{-2}$  are fit with equation (2). Examples of the fit with equation (2) and  $\alpha = 1$  to the energy distribution are shown as solid (red) lines in figure 5(a). For

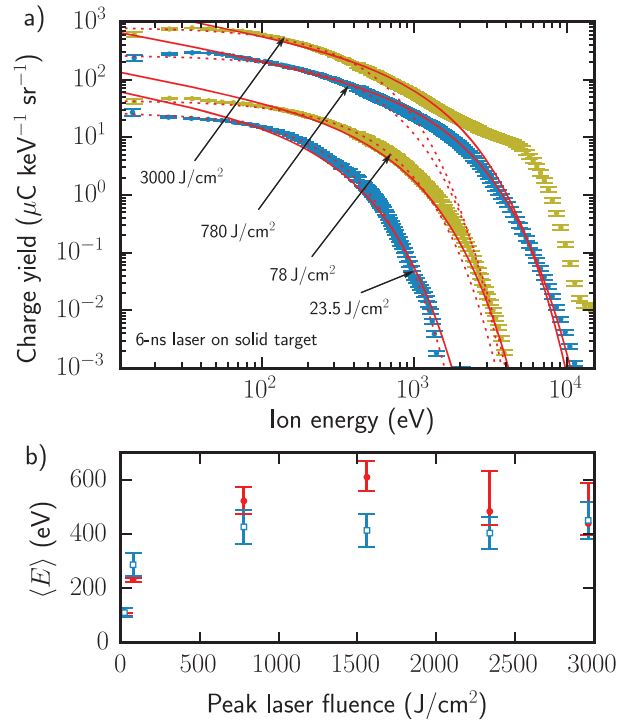


**Figure 5.** (a) Charge yield distributions for different peak fluences on the solid target and fits with equation (2) and  $\alpha = 1$  solid (red) lines,  $\alpha = 2$  dashed (dark-red) lines. (b) The values for  $\langle E \rangle$  are obtained from the fits with equation (2) for these distributions. Closed (red) circles correspond to  $\tilde{E}_0/2 = \langle E_{\text{fit}} \rangle$  for  $\alpha = 1$ , along with  $\langle E_{\text{exp}} \rangle$  (open, blue squares). Obtained values for  $\langle E_{\text{fit}} \rangle$  for  $\alpha = 2$  are omitted.

$\alpha = 2$ , the fit is illustrated by the dashed (red) lines. The energy distributions obtained with laser fluences below  $80 \text{ J cm}^{-2}$  both  $\alpha = 1$  and  $\alpha = 2$  produce good agreement with equation (2). The ion energy distribution shows a flat response below 50 eV, which is better captured by choosing  $\alpha = 2$ . At peak fluences above  $2.4 \text{ kJ cm}^{-2}$ , the energy distributions feature a ‘shoulder’ around an energy of 6 keV that is not reproduced by equation (2).

Figure 5(b) shows the average energies of ions  $\langle E_{\text{fit}} \rangle = \tilde{E}_0/2$  for  $\alpha = 1$  obtained from fitting the data to equation (2) as solid (red) circles. The open (blue) squares show the average energies obtained from the experimental data. The characteristic ion energies follow a non-linear trend saturating at a peak fluence of  $1.6 \text{ kJ cm}^{-2}$ . Then, at a higher peak fluence, the fit becomes inaccurate because of the abundance of ions with energies above 6 keV. At the lower fluences, we obtain reasonable agreement between the values  $\langle E_{\text{exp}} \rangle$  and  $\langle E_{\text{fit}} \rangle$  (see figure 5).

Our comparisons between the theoretical and measured charge-integrated energy distributions show that over a wide range of peak fluences the results of Mora [20] and Murakami *et al* [19] can be employed to characterize ion emission of LPPs. Care should be taken when laser pulses of high peak fluence are used to create LPPs. Under such conditions, the energy distributions exhibit an abundance of charges at high energies. Especially for the 6-ns pulses with

energies  $> 2.6 \text{ kJ cm}^{-2}$ , the distribution shows a peak that cannot be reproduced by either of the two model descriptions.

## 5. Conclusion

We present the ion distributions of LPPs for droplet and planar targets for various laser pulse lengths and energies, and compare them with the predictions of two results of hydrodynamic models. The charge-integrated energy distributions of ions are well explained by theoretical predictions of [19, 20]. The ion energy distributions fit well the energy distributions found by Mora [20] when the plasma is produced by laser pulses below 100 ps. In contrast, laser pulses of 6 ns duration produced expanding plasmas with ion energy distributions that can be fit by the findings of Murakami *et al* [19]. The essential difference of the expansion of plasma produced either by ultrashort pulses or ns-long pulses lies in the density evolution of the plasma during expansion. Ultrashort pulses produce plasma with an exponentially decaying density. While ultrashort pulses are off when the produced plasma expands, the ns-long pulse continues to heat the disintegrated target during part of its expansion. The density of the plasma generated in this way has a Gaussian shape, and the pressure of the plasma decreases in time. The two types of plasma expansions from LPPs may be studied in future to clarify this dynamical behavior in the transition regime by producing plasma with laser pulses between 100 ps and 6 ns.

Fitting the theoretical findings to the experimental energy distributions provides a characteristic ion energy of the expanding plasma. By performing additional charge-state resolved measurements, the actual electron temperature of the plasma, as in equation (3), may be determined. Charge state resolving ion energy spectrometry not only will enable the determination of the electron temperature, but may point at why the theoretical predictions fail to explain an abundance of high energy ions when the plasma is produced by high-peak-fluence laser pulses.

The findings of our work show that relatively simple models are sufficient to explain measured ion energy distributions of the LPPs studied here. The understanding of ion emission of expanding plasmas is an important step to assess optics damage in short-wavelength light sources.

## Acknowledgments

We thank M Basko for fruitful discussions. This work has been carried out at the Advanced Research Center for Nanolithography (ARCNL), a public-private partnership of the University of Amsterdam (UvA), the Vrije Universiteit Amsterdam, the Netherlands Organisation for Scientific Research (NWO) and the semiconductor equipment manufacturer ASML.

## ORCID iDs

A Bayerle  <https://orcid.org/0000-0002-1534-7731>

D Kurilovich  <https://orcid.org/0000-0001-7373-3318>

O O Versolato  <https://orcid.org/0000-0003-3852-5227>

## References

- [1] Cummings E A, Daily J E, Durfee D S and Bergeson S D 2005 Ultracold neutral plasma expansion in two dimensions *Phys. Plasmas* **12** 123501
- [2] Killian T C, Kulin S, Bergeson S D, Orozco L A, Orzel C and Rolston S L 1999 Creation of an ultracold neutral plasma *Phys. Rev. Lett.* **83** 4776
- [3] Flacco A, Guemnie-Tafo A, Nuter R, Veltcheva M, Batani D, Lefebvre E and Malka V 2008 Characterization of a controlled plasma expansion in vacuum for laser driven ion acceleration *J. Appl. Phys.* **104** 103304
- [4] McKenna P *et al* 2008 Effects of front surface plasma expansion on proton acceleration in ultraintense laser irradiation of foil targets *Laser Part. Beams* **26** 591
- [5] Bakshi V 2006 *EUV Sources for Lithography* (Bellingham, WA: SPIE)
- [6] Banine V Y, Koshelev K N and Swinkels G H P M 2011 Physical processes in EUV sources for microlithography *J. Phys. D: Appl. Phys.* **44** 253001
- [7] Thestrup B, Toftmann B, Schou J, Doggett B and Lunney J 2003 A comparison of the laser plume from Cu and YBCO studied with ion probes *Appl. Surf. Sci.* **208-209** 33
- [8] Toftmann B, Doggett B, Budtz-Jørgensen C, Schou J and Lunney J G 2013 Femtosecond ultraviolet laser ablation of silver and comparison with nanosecond ablation *J. Appl. Phys.* **113** 083304
- [9] Verhoff B, Harilal S and Hassanein A 2012 Angular emission of ions and mass deposition from femtosecond and nanosecond laser-produced plasmas *J. Appl. Phys.* **111** 123304
- [10] Freeman J, Harilal S, Verhoff B, Hassanein A and Rice B 2012 Laser wavelength dependence on angular emission dynamics of Nd:YAG laser-produced Sn plasmas *Plasma Sources Sci. and Technol.* **21** 055003
- [11] Farid N, Harilal S S, Ding H and Hassanein A 2013 Kinetics of ion and prompt electron emission from laser-produced plasma *Phys. Plasmas* **20** 073114
- [12] Coons R W, Campos D, Crank M, Harilal S S and Hassanein A 2014 Comparison of EUV spectral and ion emission features from laser-produced Sn and Li plasmas *Proc. SPIE* **7636** 763636
- [13] Vinokhodov A, Krivtsun V, Krivokorytov M, Sidelnikov Y, Chekalin S, Kompanets V, Melnikov A and Koshelev K 2014 Femtosecond laser pre-pulse technology for LPP EUV source *International Workshop on EUV and Soft X-Ray Sources, Dublin*
- [14] Chen Z, Wang X, Zuo D and Wang J 2016 Investigation of ion characteristics in CO<sub>2</sub> laser irradiating preformed tin-droplet plasma *Laser Part. Beams* **34** 552
- [15] Deuzeman M J *et al* 2017 Ion distribution and ablation depth measurements of a fs-ps laser-irradiated solid tin target *J. Appl. Phys.* **121** 103301
- [16] Gurevich A V, Pariiskaya L V and Pitaevskii L P 1966 Self-similar motion of rarefied plasma *J. Exp. Theor. Phys.* **22** 647
- [17] Anisimov S I, Bäuerle D and Luk'yanchuk B S 1993 Gas dynamics and film profiles in pulsed-laser deposition of materials *Phys. Rev. B* **48** 12076
- [18] Doggett B and Lunney J 2011 Expansion dynamics of laser produced plasma *J. Appl. Phys.* **109** 093304

- [19] Murakami M, Kang Y, Nishihara K, Fujioka S and Nishimura H 2005 Ion energy spectrum of expanding laser-plasma with limited mass *Phys. Plasmas* **12** 062706
- [20] Mora P 2003 Plasma expansion into a vacuum *Phys. Rev. Lett.* **90** 185002
- [21] Bulgakova N M, Bulgakov A V and Bobrenok O F 2000 Double layer effects in laser-ablation plasma plumes *Phys. Rev. E* **62** 5624
- [22] Murakami M and Basko M 2006 Self-similar expansion of finite-size non-quasi-neutral plasmas into vacuum: relation to the problem of ion acceleration *Phys. Plasmas* **13** 012105
- [23] Crow J E, Auer P L and Allen J E 1975 The expansion of a plasma into a vacuum *J. Plasma Phys.* **14** 65
- [24] Sack C and Schamel H 1987 Plasma expansion into vacuum: a hydrodynamic approach *Phys. Rep.* **156** 311
- [25] Arefiev A V and Breizman B N 2009 Collisionless plasma expansion into vacuum: two new twists on an old problem *Phys. Plasmas* **16** 055707
- [26] Bennaceur-Doumaz D, Bara D and Djebli M 2015 Self-similar two-electron temperature plasma expansion into vacuum *Laser Part. Beams* **33** 723
- [27] Fujioka S *et al* 2005 Properties of ion debris emitted from laser-produced mass-limited tin plasmas for extreme ultraviolet light source applications *Appl. Phys. Lett.* **87** 241503
- [28] Thum-Jäger A and Rohr K 1999 Angular emission distributions of neutrals and ions in laser ablated particle beams *J. Phys. D: Appl. Phys.* **32** 2827
- [29] Apiñaniz J I, Peralta Conde A and de Mendiola R M P 2015 Experimental observation of the ion energy spectra of Al, Co, and Cu laser produced plasmas *Eur. Phys. J. D* **69** 265
- [30] Landau L and Lifshitz L 1987 *Fluid Mechanics* (Oxford: Pergamon)
- [31] London R and Rosen M 1986 Hydrodynamics of exploding foil x-ray lasers *Phys. Fluids* **29** 3813
- [32] Robicheaux F and Hanson J D 2003 Simulated expansion of an ultra-cold, neutral plasma *Phys. Plasmas* **10** 2217
- [33] Pelah I 1976 Diagnosis of laser produced plasma with charge collectors *Phys. Lett. A* **59** 348
- [34] Kurilovich D, Klein A L, Torretti F, Lassise A, Hoekstra R, Ubachs W, Gelderblom H and Versolato O O 2016 Plasma propulsion of a metallic microdroplet and its deformation upon laser impact *Phys. Rev. Appl.* **6** 014018
- [35] Bäuerle D 2011 *Laser Processing and Chemistry* (Berlin: Springer)
- [36] Thum-Jäger A, Sinha B K and Rohr K P 2000 Time of flight measurements on ion-velocity distribution and anisotropy of ion temperatures in laser plasmas *Phys. Rev. E* **63** 016405
- [37] Chen Z, Wang X, Zuo D, Lu P and Wang J 2016 Investigation of nd:YAG laser produced tin droplet plasma expansion *Laser Phys. Lett.* **13** 056002
- [38] Basko M M and Tsygvintsev I P 2017 A hybrid model of laser energy deposition for multi-dimensional simulations of plasmas and metals *Comp. Phys. Comm.* **214** 59
- [39] Cisneros G, Helman J S and Wagner C N J 1982 Dielectric function of liquid tin between 250 and 1100°C *Phys. Rev. B* **25** 4248
- [40] Golovashkin A I, Levchenko I S, Motulevich G P and Shubin A A 1967 Optical properties of indium *JETP* **24** 1622